

# Crustal structure of central Tibet as derived from project INDEPTH wide-angle seismic data

W. Zhao,<sup>1</sup> J. Mechie,<sup>2</sup> L. D. Brown,<sup>3</sup> J. Guo,<sup>1</sup> S. Haines,<sup>4</sup> T. Hearn,<sup>5</sup>  
S. L. Klemperer,<sup>4</sup> Y. S. Ma,<sup>5</sup> R. Meissner,<sup>6</sup> K. D. Nelson,<sup>7</sup> J. F. Ni,<sup>5</sup> P. Pananont,<sup>3</sup>  
R. Rapine,<sup>5</sup> A. Ross<sup>3</sup> and J. Saul<sup>2</sup>

<sup>1</sup>Chinese Academy of Geological Sciences, 26 Baiwanzhuang Road, Beijing 100037, China

<sup>2</sup>GeoForschungsZentrum Potsdam (GFZ), Telegrafenberg, 14473 Potsdam, Germany. E-mail: jimmy@gfz-potsdam.de

<sup>3</sup>Department of Geological Sciences, Cornell University, Ithaca, NY 14853, USA

<sup>4</sup>Department of Geophysics, Stanford University, Stanford, CA 94305, USA

<sup>5</sup>Department of Physics, New Mexico State University, Las Cruces, NM 88003, USA

<sup>6</sup>Institut für Geowissenschaften, Kiel University, Otto-Hahn-Platz 1-2, 24118 Kiel, Germany

<sup>7</sup>Department of Earth Sciences, Syracuse University, Syracuse, NY 13244, USA

Accepted 2000 December 4. Received 2000 December 1; in original form 2000 May 1

## SUMMARY

In the summer of 1998, project INDEPTH recorded a 400 km long NNW–SSE wide-angle seismic profile in central Tibet, from the Lhasa terrane across the Banggong–Nujiang suture (BNS) at about 89.5°E and into the Qiangtang terrane. Analysis of the *P*-wave data reveals that (1) the crustal thickness is  $65 \pm 5$  km beneath the line; (2) there is no 20 km step in the Moho in the vicinity of the BNS, as has been suggested to exist along-strike to the east based on prior fan profiling; (3) a thick high-velocity lower crustal layer is evident along the length of the profile (20–35 km thick, 6.5–7.3 km s<sup>-1</sup>); and (4) in contrast to the southern Lhasa terrane, there is no obvious evidence of a mid-crustal low-velocity layer in the *P*-wave data, although the data do not negate the possibility of such a layer of modest proportions.

Combining the results from the INDEPTH III wide-angle profile with other seismic results allows a cross-section of Moho depths to be constructed across Tibet. This cross-section shows that crustal thickness tends to decrease from south to north, with values of 70–80 km south of the middle of the Lhasa terrane, 60–70 km in the northern part of the Lhasa terrane and the Qiangtang terrane, and less than 60 km in the Qaidam basin. The overall northward thinning of the crust evident in the combined seismic observations, coupled with the essentially uniform surface elevation of the plateau south of the Qaidam basin, is supportive of the inference that northern Tibet until the Qaidam basin is underlain by somewhat thinner crust, which is isostatically supported by relatively low-density, hot upper mantle with respect to southern Tibet.

**Key words:** crustal structure, seismic modelling, Tibetan plateau.

## INTRODUCTION

During the summer of 1998, within the framework of the INDEPTH III project, seismic refraction/wide-angle reflection data were recorded from large shots along a 400 km long NNW–SSE profile crossing the Banggong–Nujiang suture (BNS) at about 89.5°E in central Tibet (Fig. 1). The main purpose of the wide-angle seismic measurements was to obtain a crustal velocity model for central Tibet and thus provide a contribution to the knowledge of the structure and evolution of the plateau as a whole. A total of almost 60 three-component

broadband and short-period stand-alone seismographs, mainly at a spacing of 5–10 km, and a 60-channel Geometrics system equipped with vertical component geophones recorded 11 large shots with charge sizes ranging from 180 to 1160 kg. In addition, the same seismographs recorded, also at near-vertical angles of incidence, four in-line groups and one cross-line group of small shots with charge sizes ranging from 2 to 50 kg. Following the active source experiment, 57 three-component stand-alone seismographs, including eight that were not located along the NNW–SSE profile, were left until the summer of 1999 to record earthquakes. This contribution will present

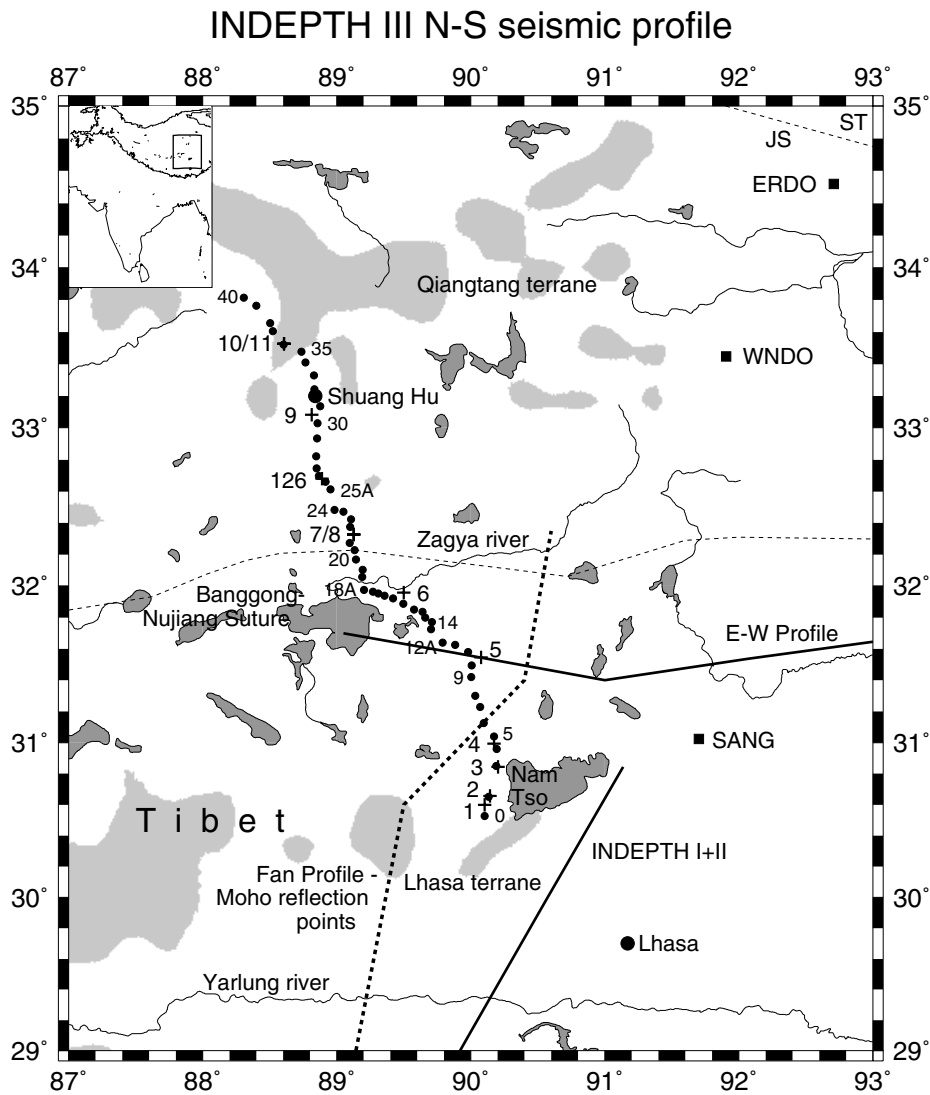


**Figure 1.** Location map (box within the inset) for the INDEPTH III N-S seismic profile in central Tibet. Crosses and larger numbers represent shots, while filled circles and smaller numbers represent recording stations. The locations of the INDEPTH I+II traverse (Alsdorf *et al.* 1998a), the E-W profile of Sapin *et al.* (1985), the Moho reflection points of the fan profile of Hirn *et al.* (1984a), and three broadband stations (SANG, WNDO, ERDO) for which crustal structure has been obtained are also shown. JS: Jinsha river suture; ST: Songpan-Ganzu terrane. The whole of the INDEPTH III seismic profile lies above 4500 m. Ground above 5500 m is shaded light grey, while lakes are shaded dark grey. In the inset the outline of the Tibet plateau, as defined by the 3000 m contour, is shown.

results obtained from modelling the *P*-wave refraction/wide-angle reflection data recorded from the 11 large shots and one small shot (126) along the 400 km long NNW-SSE profile. No modelling of *S* waves is shown as the large shots failed to produce significant *S*-wave energy, even on the horizontal components.

The BNS is thought to have formed during the Late Jurassic-Early Cretaceous as a consequence of the collision between the Lhasa and Qiangtang terranes, with the latter comprising the southern margin of Asia immediately prior to the collision (Allègre *et al.* 1984; Girardeau *et al.* 1984; Dewey *et al.* 1988). Recent geological mapping (Murphy *et al.* 1997) has indicated that the northern Lhasa terrane was shortened by as much as 60 per cent during or subsequent to the Lhasa-Qiangtang collision, but prior to the collision of India with the southern margin of the Lhasa terrane at about 50 Ma. The magnitude of shortening of the Qiangtang terrane attributable to

any of the Tibetan collisional events is unknown. From south to north the principal bedrock units crossed by the INDEPTH III profile are the Cretaceous-Tertiary Nam Tso thrust belt, the middle Cretaceous Baingoin batholith, the Cenozoic Duba and Lumpola basins, the surface trace of the BNS, folded Jurassic-Cretaceous strata of the southern Qiangtang terrane, and the Neogene Shuang Hu graben (Kidd *et al.* 1988; Xia *et al.* 1993).

Previous seismic work in the vicinity of the BNS includes a 500 km long E-W wide-angle seismic profile in the northern Lhasa terrane just south of the BNS. The recording sites along the western 90 km of this profile more or less coincide with those of the INDEPTH III profile between sites 18 A and 11 (Fig. 1), after which the two profiles diverge. From this profile a crustal thickness of about 70 km was derived (Sapin *et al.* 1985). From fan profiling with Moho reflection points along an approximately NNE-SSW-trending line (Fig. 1), Hirn *et al.* (1984a) postulated a 20 km step in the Moho across the BNS

about 100 km east of the INDEPTH III profile. From a N–S wide-angle seismic profile about 500 km west of the INDEPTH III profile, Kong *et al.* (1996) obtained crustal thicknesses of 70–75 km and 65–70 km for the northern Lhasa and southern Qiangtang terranes, respectively, and a small change in Moho depths of about 4 km in the vicinity of the BNS.

From an analysis of teleseismic shear-coupled *P* waves recorded by the 1991–1992 Sino-American broadband experiment across the Tibetan plateau, Owens & Zandt (1997) derived velocity–depth functions for the northernmost Lhasa terrane (seismic station SANG, Fig. 1), the Qiangtang terrane (station WNDO, Fig. 1) and the Songpan-Ganz terrane (station ERDO, Fig. 1). This analysis obtained crustal thicknesses of 74 km for the northernmost Lhasa terrane, 65 km for the Qiangtang terrane and 55 km for the Songpan-Ganz terrane. Utilizing data also from the 1991–1992 Sino-American broadband experiment across the Tibetan plateau and a variation of the receiver function method, Zhao *et al.* (1996) derived crustal thicknesses of 65–75 km for station SANG, about 65 km for station WNDO and about 70 km for station ERDO. From observations of regional waveforms also recorded by the 1991–1992 Sino-American broadband experiment, Rodgers & Schwartz (1997, 1998) derived a crustal thickness of about 70 km and an average crustal *P*-wave velocity of 5.9–6.1 km s<sup>-1</sup> for paths mainly through the Lhasa terrane in southern Tibet, and a crustal thickness of 65 ± 5 km and an average crustal *P*-wave velocity of 6.1–6.3 km s<sup>-1</sup> for the Qiangtang terrane.

## DATA AND PHASE CORRELATIONS

Figs 2 to 6 show, for each of the shot-points 3, 4, 6, 9 and 10 along the profile, the compressional (*P*) seismic wavefield recorded by the vertical component of the instruments at each receiver position. These shot gathers are displayed in the form of distance versus reduced-time record sections, in which each trace has been bandpass filtered (2–12 Hz) and normalized with respect to its own maximum amplitude. A reduction velocity of 8 km s<sup>-1</sup> has been utilized as this provides the best overall display of the data and, in particular, of the reflected phase from the crust–mantle boundary. It also facilitates comparison with other data from Tibet, which have also been displayed using a reduction velocity of 8 km s<sup>-1</sup> (Hirn *et al.* 1984b). Traveltimes calculated from the derived model (Figs 7 and 8) are superimposed on the record sections, together with the observed traveltimes.

The record sections from shots 3 and 4 (Figs 2 and 3) towards the southern end of the profile are very similar in nature. The average apparent velocity of the first arrival phase, *P*<sub>g</sub>, between 20 and 200 km distance is 5.7–5.8 km s<sup>-1</sup>. In both record sections at the Zagya river (at about 145 km distance from shot 4 and about 160 km distance from shot 3), about 25 km south of the BNS, there is an apparent breakdown in the energy of the first arrivals, which thus become difficult to pick. An intracrustal reflected phase, *Pi1P*, is quite well seen between 90 and 160 km distance in both record sections. The reflected

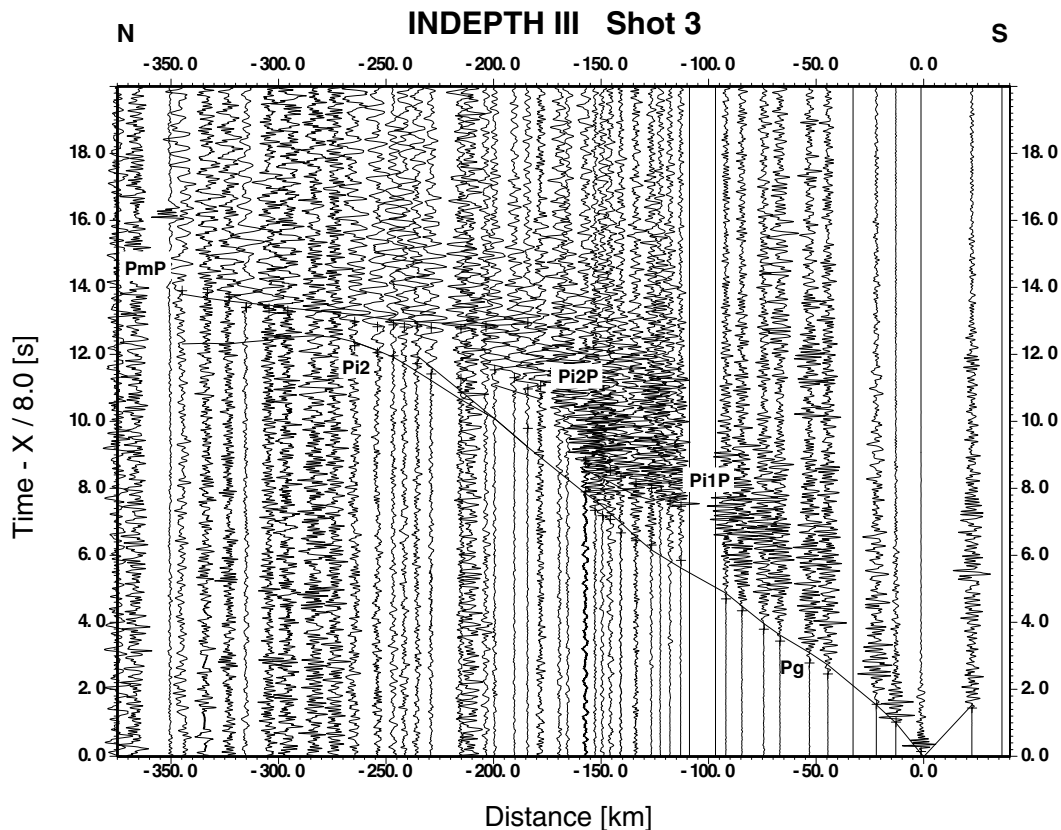


**Figure 2.** Seismic data from shot 3 along the INDEPTH III profile. The record section reduced with a velocity of 8 km s<sup>-1</sup> shows the vertical component of *P*-wave motion in which each trace is normalized individually and bandpass filtered from 2 to 12 Hz. Continuous lines represent phases calculated from the model in Fig. 7, while crosses represent traveltimes picks. Key: *P*<sub>g</sub>: first arrival refraction through the upper crust; *Pi1P*: reflection from the top of the middle crust; *Pi2P*: reflection from the top of the lower crust; *Pi2*: first arrival refraction through the lower crust; *PmP*: reflection from the Moho.

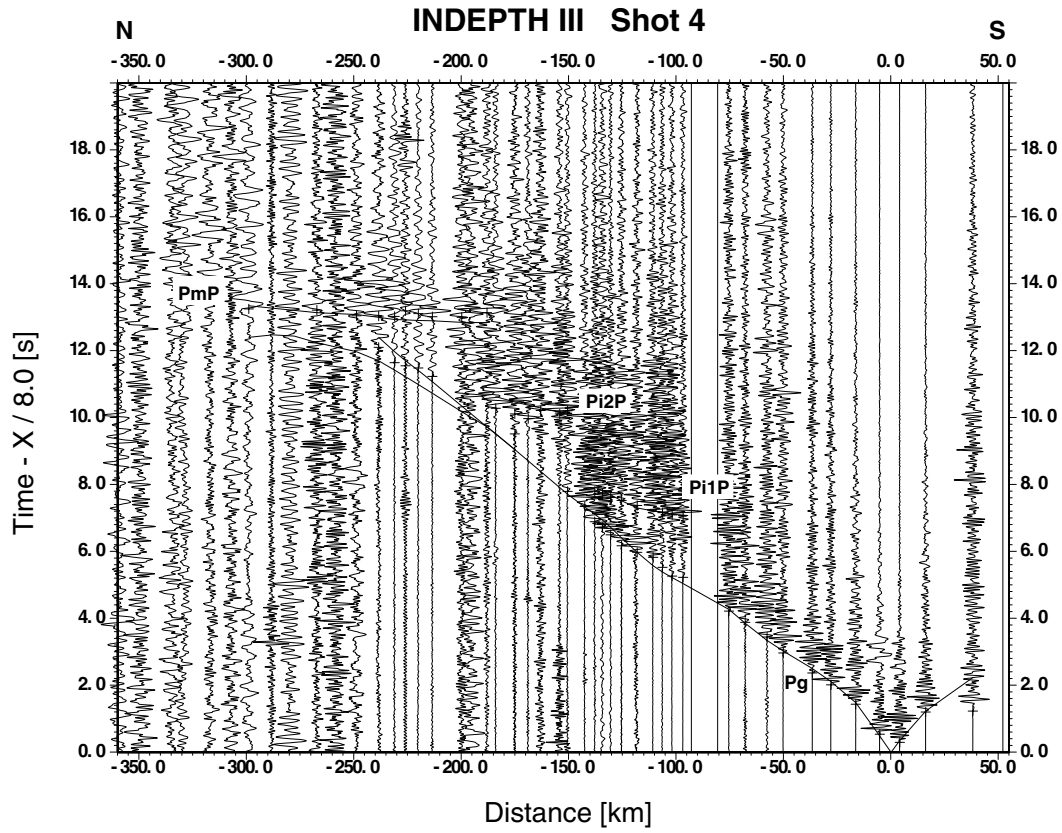


Figure 3. Seismic data from shot 4 along the INDEPTH III profile. The data are processed and presented as in Fig. 2. Key: see Fig. 2.

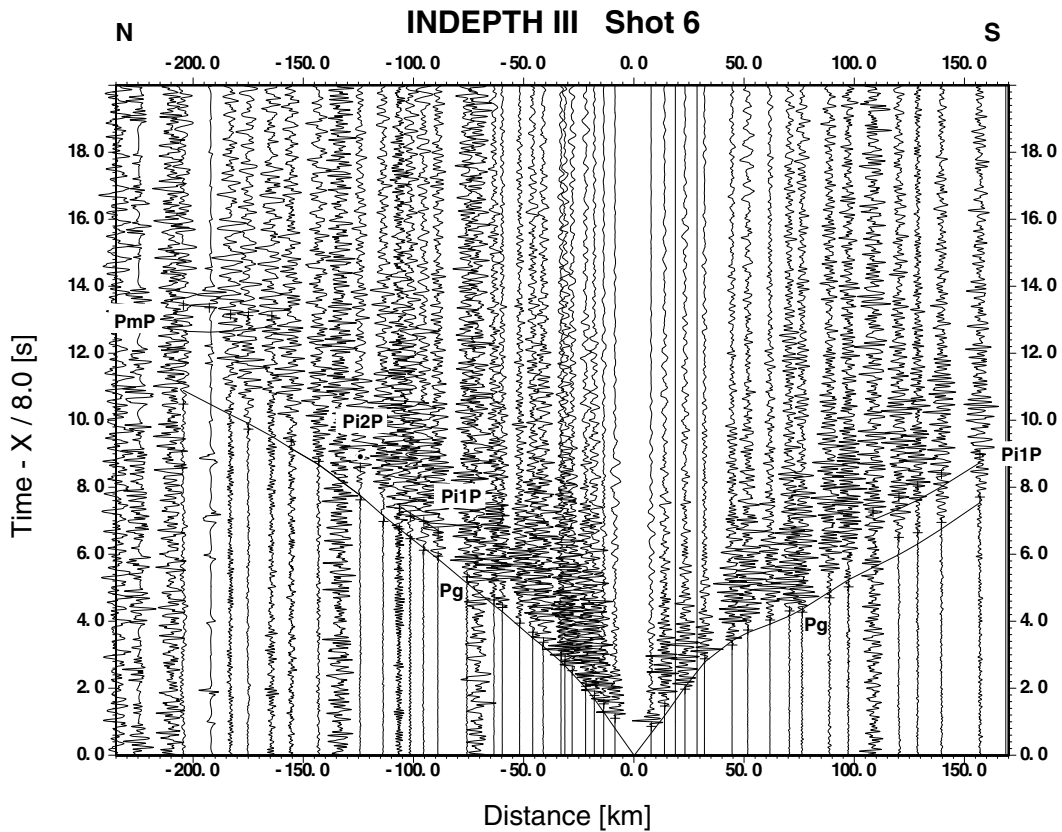


Figure 4. Seismic data from shot 6 along the INDEPTH III profile. The data are processed and presented as in Fig. 2. Key: see Fig. 2.

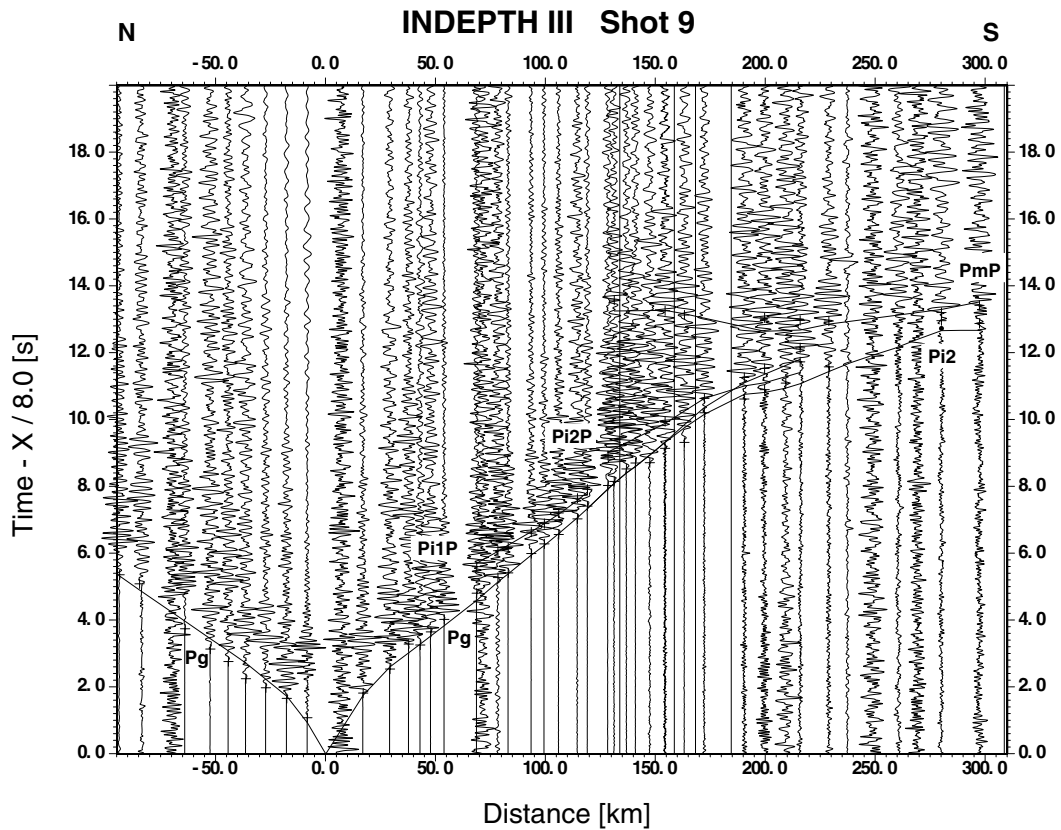


Figure 5. Seismic data from shot 9 along the INDEPTH III profile. The data are processed and presented as in Fig. 2. Key: see Fig. 2.

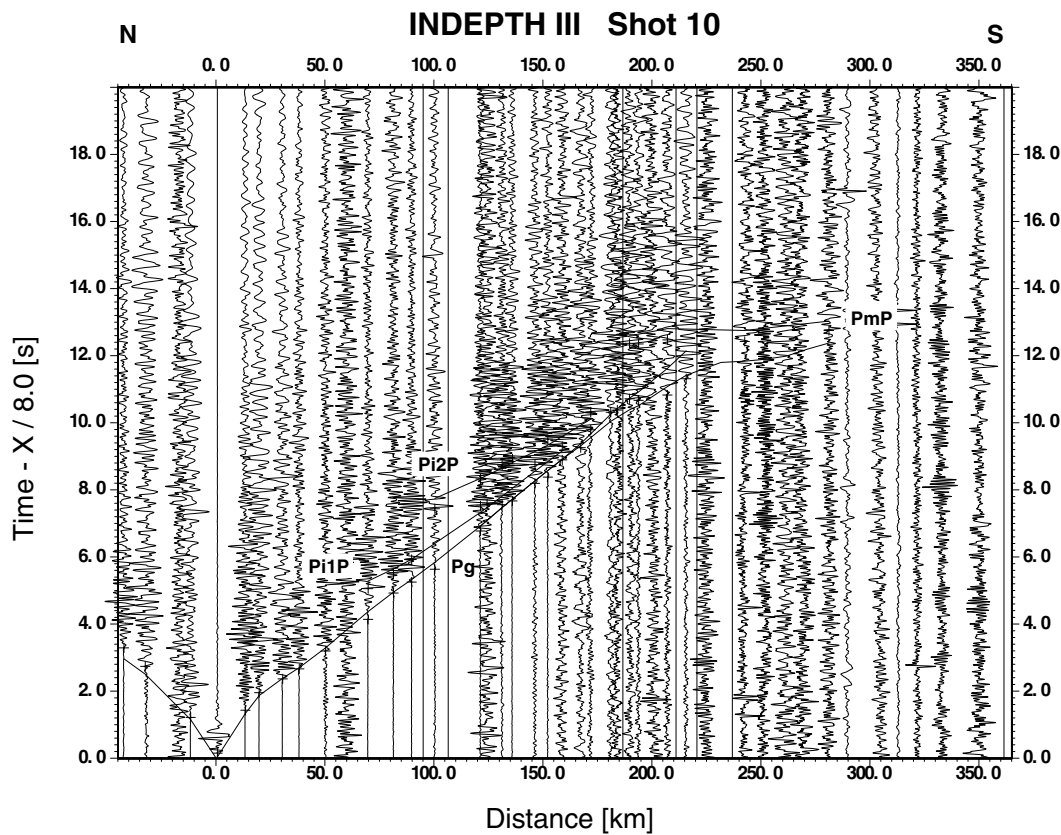


Figure 6. Seismic data from shot 10 along the INDEPTH III profile. The data are processed and presented as in Fig. 2. Key: see Fig. 2.

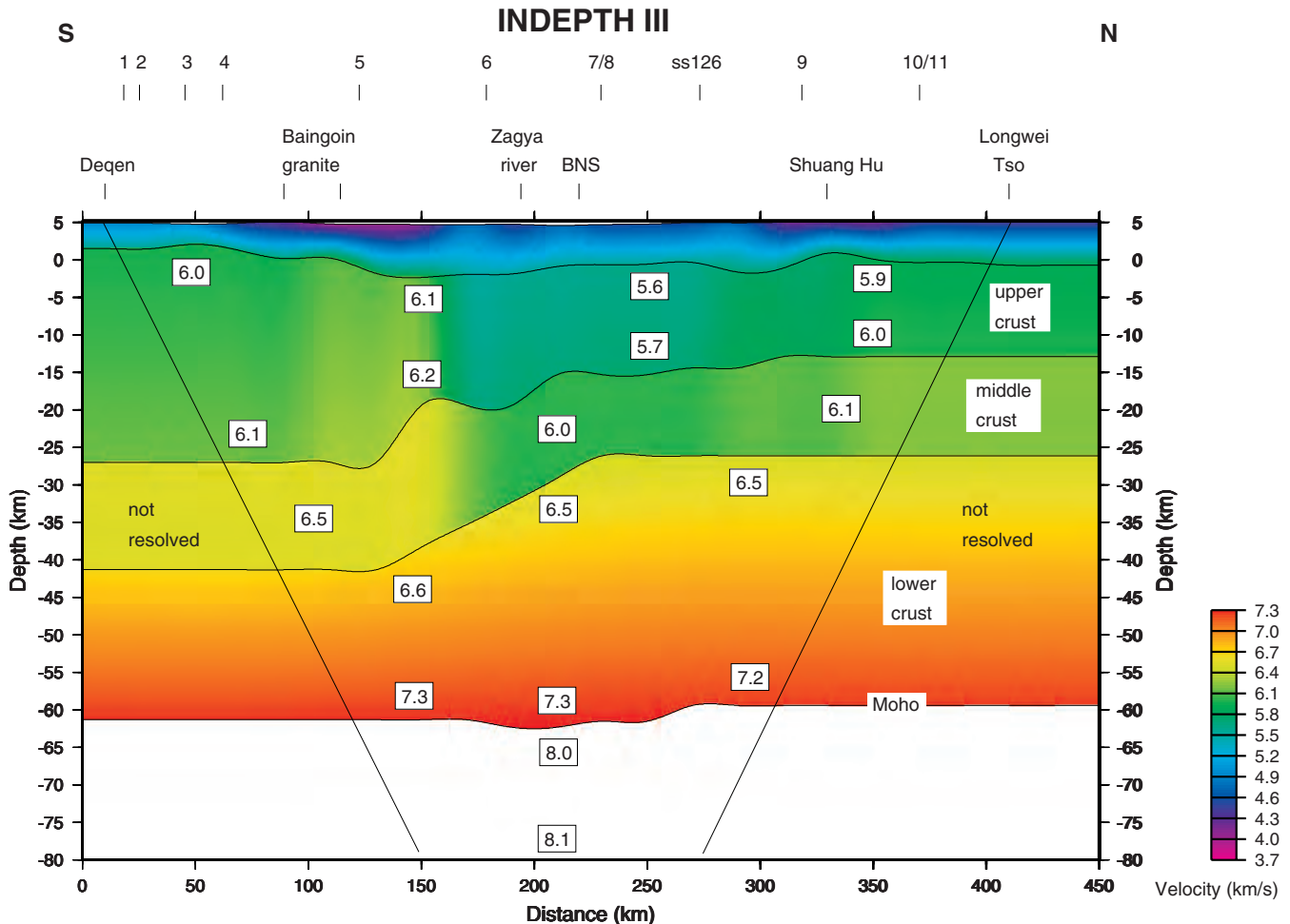


Figure 7. *P*-wave velocity model for the INDEPTH III profile in central Tibet. Velocities are in  $\text{km s}^{-1}$ . BNS: Banggong-Nujiang suture.

phase, *PmP*, from the crust–mantle boundary (Moho) is well observed between 200 and 350 km distance. On the record section from shot 3 the outer end of the *PmP* phase at 300–350 km distance has a high apparent velocity of about  $7.3 \text{ km s}^{-1}$ , and some first arrivals at about 250 km distance also have an apparent velocity well in excess of  $6 \text{ km s}^{-1}$ . The above two observations and the observation of some large-amplitude secondary arrivals from both shots at 150–200 km distance, correlated as representing an intracrustal reflected phase, *Pi2P*, indicate the existence of a high-velocity lower crustal layer. The refracted phase, *Pn*, through the uppermost mantle is not observed on any record section. However, the apparent velocity of the *PmP* phase at the critical distance of about 200 km is close to  $8 \text{ km s}^{-1}$ , and the apparent velocity of the *Pn* phase from two local earthquakes located north and south of the profile, respectively, is also about  $8 \text{ km s}^{-1}$ . Shot 2 is similar in nature to shots 3 and 4 but of poorer quality, while from shot 1 only some first arrivals out to about 100 km distance can be seen.

The record section from shot 6 (Fig. 4) located just south of the BNS shows clear first arrivals out to the southern end of the profile and out to about 200 km distance towards the north. Towards the south the first arrival phase, *Pg*, has an average apparent velocity of  $6.0\text{--}6.1 \text{ km s}^{-1}$ , whereas towards the north

the value is  $5.7\text{--}5.8 \text{ km s}^{-1}$ . Between 100 and 150 km distance south of the shot, an intracrustal reflected phase, *Pi1P*, can be correlated 1–1.5 s behind the first arrivals. At around 100 km distance north of the shot, a few arrivals pertaining to the same phase can be recognized 0.5–1 s behind the first arrivals. Beyond 160 km distance towards the north some *PmP* reflections can be seen. Shot 5, located about 55 km south of shot 6, is very similar in nature but of poorer quality and does not, for example, show any *PmP* reflections. From shots 7 and 8 at the same location about 50 km north of shot 6, and from the small shot 126 about 45 km further north, only first arrivals can be picked.

The record sections from shots 9 and 10 (Figs 5 and 6) towards the northern end of the profile are also similar in nature, but are different from those from shots 3 and 4. The average apparent velocity of the first arrival phase, *Pg*, is  $5.6\text{--}5.8 \text{ km s}^{-1}$  between 20 and 150 km distance. On both record sections, about 0.5–1 s behind the first arrivals and between 60 and 160 km distance, an intracrustal reflected phase, *Pi1P*, can be correlated. At later times a second intracrustal reflected phase, *Pi2P*, has been recognized, characterized by a prominent burst of energy on some traces between 100 and 200 km distance. *PmP* is the dominant phase beyond about 220 km distance. At smaller distances it is characterized by a prominent burst of

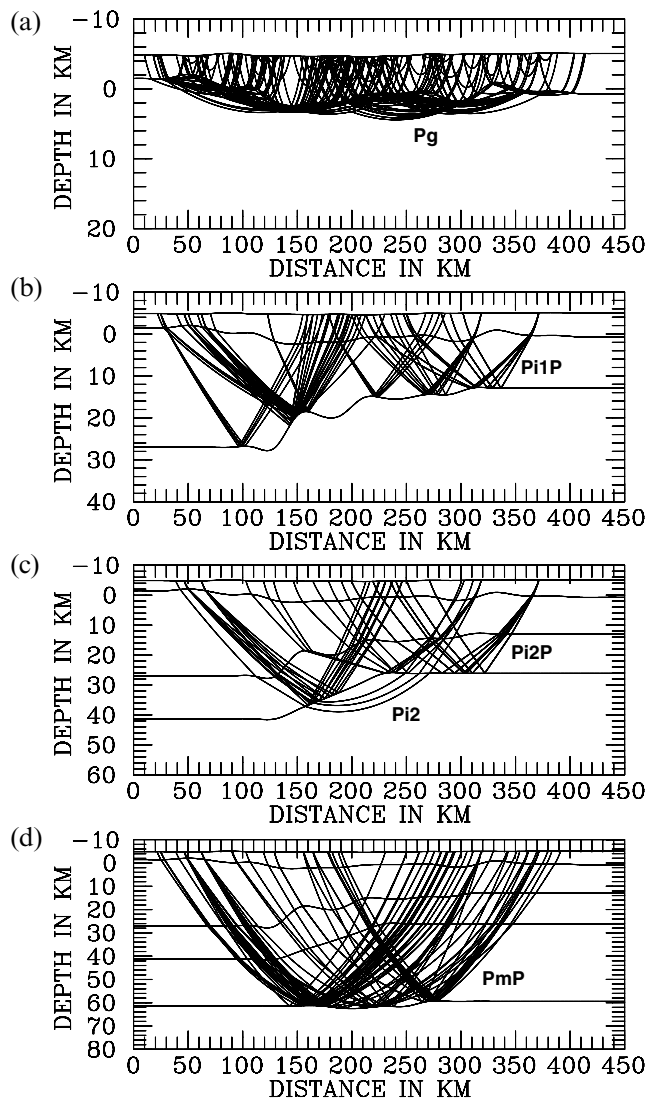


Figure 8. Ray diagrams for the final iterations of (a) the  $P_g$  phase, (b) the  $Pi1P$  phase, (c) the  $Pi2P$  and  $Pi2$  phases, and (d) the  $PmP$  phase.

energy on a reasonable number of traces. On the record section from shot 9 at the furthest offsets of about 300 km, the  $PmP$  phase has a high apparent velocity in excess of  $7.0 \text{ km s}^{-1}$ . Shot 11, executed at the same position as shot 10, was somewhat weaker. The stacked record section from both shots did not bring any significant improvement to the signal/noise ratio, and the phase onsets tended to be less well defined.

One of the main differences between the record sections from shots 9 and 10 on the one hand and shots 3 and 4 on the other is that there is no apparent breakdown in the energy of the first arrivals at the Zagya river (at about 125 km distance from shot 9 and about 175 km distance from shot 10), about 25 km south of the BNS, on the record sections from shots 9 and 10. A further difference is that the  $PmP$  phase is not so prominent on the record sections from the northern two shots. Finally, the intracrustal reflection,  $Pi1P$ , occurs closer behind the first arrivals and at smaller distances from the northern two shots, indicating that the interface associated with this reflection occurs at smaller depths under the northern part of the profile than it does under the southern part.

## MODELLING

In order to interpret the phase correlations described above, the arrival times were first picked and then 1-D velocity–depth models were constructed for each shot in each of the two directions using both traveltimes and amplitudes. These 1-D models were then combined to provide starting models, of varying degrees of complexity, for the derivation of a 2-D velocity model. The 1-D velocity–depth models were calculated using trial-and-error forward modelling in which theoretical traveltimes were calculated using ray tracing (see, for example, Červený *et al.* 1977), and theoretical amplitudes were calculated using the reflectivity method (Fuchs & Müller 1971). The 2-D model was derived using a combination of trial-and-error forward modelling of traveltimes and amplitudes, and inverse modelling of traveltimes. For the traveltime modelling, the forward problem was solved by classical ray-tracing techniques (Červený *et al.* 1977) for the reflected phases, and finite-difference ray tracing based on the eikonal equation (Vidale 1988; Podvin & Lecomte 1991; Schneider *et al.* 1992) for the first arrival refracted phases. Partial derivatives of the calculated traveltimes with respect to the velocity and interface nodes were then derived using the techniques described by Lutter & Nowack (1990), Lutter *et al.* (1990) and Zelt & Smith (1992). Subsequently, a damped least-squares inversion (see, for example, Zelt & Smith 1992) was carried out to obtain updates for the velocity and interface nodes, and the forward and inverse problems were repeated until an acceptable convergence between the observed and calculated traveltimes was obtained.

The traveltime modelling was done using a top-to-bottom approach in four major steps (upper crust, middle crust, lower crust, Moho), as described below. In total, 417 traveltime readings were used in the inversion (Table 1), and the model contains 32 independent velocity and interface depth parameters (Tables 2 and 3). Although the velocities and interface depths in the model were usually specified at 20 km intervals (90 km intervals in the case of the velocities in the lower crustal layer) along the profile, in the inversion a smaller number of independent velocity and depth parameters was solved for by grouping the individual nodes together (Table 2). To supplement and guide the traveltime modelling, amplitudes were calculated at the end of the second and fourth steps using a finite-difference approximation of the wave equation for 2-D heterogeneous elastic media by Kelly *et al.* (1976) with transparent boundary conditions (Reynolds 1978) and implemented by Sandmeier (1990).

### Step 1: upper crustal structure

In the first step, 260 first arrival traveltimes (Table 1) out to distances generally of around 160 km were inverted in order to obtain the velocity structure of the top two layers and the structure of the first interface (Figs 7 and 8a). As there are only a small number of rays that only penetrate the top layer and thus effectively define the velocity of the top layer, laterally varying top-layer velocities derived from the 1-D velocity–depth modelling were used in the 2-D starting model. Furthermore, as the velocity contrast at the first interface is often relatively small, laterally varying depths for the first interface, again derived from the 1-D velocity–depth modelling, were used in the 2-D starting model. For the second top layer, uniform velocities of

**Table 1.** Number of traveltimes picked for each phase from each shot. In the case of the *Pg* and 1st arr., the maximum distances (in km) for which an arrival was picked are also given.

Shot	1	2	3	4	5	6	7	8	126	9	10	11	10+11	Total
Phase														
<i>Pg</i>	7 95	14 140	18 160	21 150	26 130	36 160	17 85N 80S	18 160N 75S	20 90	29 160	19 160	17 160	18 160	260
1st arr.	7 95	20 215	23 250	28 240	29 180	38 205	25 85N 210S	25 160N 195S	20 95	36 230	27 215	22 215	26 285	326
<i>Pi1P</i>		8	7	8	4	9				8	7	6	7	64
<i>Pi2P</i>			4	6		1				6	6	6	5	34
<i>Pi2</i>			2							1				3
<i>PmP</i>		5	15	10		5				8	5	5	3	56

6.00 km s<sup>-1</sup> at the top and 6.15 km s<sup>-1</sup> at the bottom of the layer were used in the 2-D starting model. The velocities at the top and bottom of each individual layer were constrained to be updated by the same amount in each iteration of the inversion. In the inversion only six independent velocity

nodes in each layer, each with an *a priori* uncertainty estimate of  $\pm 0.5$  km s<sup>-1</sup>, were utilized. In addition, eight independent depth nodes on the interface, each with an *a priori* uncertainty estimate of  $\pm 5$  km, were employed, making a total of 20 model parameters to be solved for (Tables 2 and 3).

**Table 2.** Some input parameters for the inversion and the resolution (*R*) for the various nodes for the final iteration.

Parameter type	no. of nodes	<i>R</i>	node coordinates (km)
top layer velocity	6	0.47	0, 10, 30, 50, 70, 90
		0.41	110, 130, 150
		0.47	170, 190, 210
		0.38	230, 250, 270
		0.49	290, 310, 330
		0.54	350, 370, 390, 410, 430, 450
2nd layer velocity	6	0.71	0, 10, 30, 50, 70, 90
		0.70	110, 130, 150
		0.68	170, 190, 210
		0.80	230, 250, 270
		0.75	290, 310, 330
		0.40	350, 370, 390, 410, 430, 450
1st interface	8	0.31	0, 10, 30
		0.46	50, 70, 90
		0.28	110, 130, 150
		0.15	170, 190, 210
		0.16	230, 250, 270
		0.15	290, 310, 330
		0.13	350, 370, 390
		0.06	410, 430, 450
<i>Pi1P</i> interface	5	0.23	0, 10, 30, 50, 70, 90, 110, 130
		0.72	150, 170, 190
		0.26	210, 230, 250
		0.43	270, 290
		0.51	310, 330, 350, 370, 390, 410, 430, 450
<i>Pi2P</i> interface	2	0.53	0, 10, 30, 50, 70, 90, 110, 130, 150, 170, 190
		0.66	210, 230, 250, 270, 290, 310, 330, 350, 370, 390, 410, 430, 450
<i>Pi2</i> velocity	1	0.24	0, 90, 180, 270, 360, 450
<i>PmP</i> interface	4	0.45	0, 10, 30, 50, 70, 90, 110, 130, 150, 170
		0.09	190, 210
		0.28	230, 250
		0.57	270, 290, 310, 330, 350, 370, 390, 410, 430, 450

**Table 3.** Some input parameters and results of the inversion.  $\sigma_d$  is the standard deviation of the traveltime readings,  $\sigma_m$  is the *a priori* uncertainty in the model parameters, and  $D$  is the overall damping factor (see, for example, Zelt & Smith 1992).

Phase	$P_g$	$P_{i1P}$	$P_{i2P}/P_{i2}$	$P_{mP}$
parameter				
ave. $\Delta t$ start model (s)	0.62	0.66	0.30	0.29
ave. $\Delta t$ final model (s)	0.18	0.24	0.26	0.27
$\sigma_d$ (s)	0.1	0.2	0.2	0.2
$\sigma_m$ -interface (km)	5.0	5.0	5.0	5.0
$\sigma_m$ -velocity ( $\text{km s}^{-1}$ )	0.5		0.3	
$D$	400	100	100	100

After nine iterations, the average absolute difference between the theoretical and observed traveltimes had decreased from 0.62 s to 0.18 s with no further significant improvement occurring. The ray diagram (Fig. 8a) gives an indication of which regions of the model are well constrained. Inspection of the resolution matrix shows that the velocity nodes in the second layer are usually well resolved, with resolution values of 0.68–0.80, except for the northernmost node. The velocity nodes in the top layer are less well resolved, with values of 0.38–0.54, while the interface nodes are only poorly resolved with nearly all the values below 0.35. Off-diagonal elements of the resolution matrix are small in comparison with the diagonal elements for all the velocity nodes, but this is not the case for the interface nodes. It is thought that the poor resolution of the interface is due to the fact that the velocity contrast across the interface is often relatively small. As stated above this was also the reason why, in the 2-D starting model, laterally varying interface depths derived from the 1-D modelling were utilized. In the final model the general shape of the interface has not changed much with respect to the starting model.

One of the most significant results of the modelling of the upper crustal structure is the lateral variation in the  $P_g$  velocities of the second layer. Evidence for this lateral variation can actually be seen in the record sections. For example, the apparent velocities for the  $P_g$  phase on the record sections from shots 3 and 4 recorded to the north and from shot 6 recorded to the south (Figs 2 to 4) are higher than those on the record sections from shot 6 recorded to the north and shots 9 and 10 recorded to the south (Figs 4 to 6). Alternative starting models with laterally varying velocities for the second layer as derived from the 1-D modelling, a different parametrization of the independent velocity nodes in the second layer, and a smaller *a priori* uncertainty in the velocity of the second layer of only  $\pm 0.2 \text{ km s}^{-1}$  gave very similar results to the model shown here (Fig. 7). The most prominent lateral change in velocity in the second layer occurs near the Zagya river, about 25 km south of the surface trace of the Banggong-Nujiang suture, and the region of low velocities in the second layer passes beneath the surface trace of the suture and extends northwards for a further 50–70 km.

### Step 2: middle crustal structure

In step 2 the depths of the interface associated with the intracrustal reflection,  $P_{i1P}$ , were determined by inverting 64 traveltime readings for this phase (Table 1). In addition, the velocities in the layer below the interface were derived by trial-and-error

forward modelling of both amplitudes and traveltimes. The 2-D starting model consisted of a horizontal interface at an average depth of about 23 km below the surface. Five independent interface nodes, each with an *a priori* uncertainty of  $\pm 5$  km, were employed in the inversion, which after seven iterations had reduced the average absolute traveltime residual from 0.66 s in the starting model to 0.24 s, with no significant further improvement being evident (Tables 2 and 3). The interface nodes are variably well resolved, with the resolution correlating with the number of rays hitting the interface in the region of the respective node (see Fig. 8b). The off-diagonal elements of the resolution matrix are, however, all small with respect to the diagonal elements.

The most striking feature from the modelling of the interface associated with the  $P_{i1P}$  reflection is the large depth change of the interface, of about 8 km, between model km 130 and 150. This reflects the fact that the traveltime gap between the first arrivals and the  $P_{i1P}$  reflection is significantly greater on the record sections from shots 3 and 4 (Figs 2 and 3) than on those from shots 9 and 10 (Figs 5 and 6). Whether the two segments of the interface are actually continuous as shown here or whether they represent two different interfaces which perhaps die out laterally can not really be determined with the available data. The model with the smallest number of interfaces is shown here.

There are two competing effects with respect to the velocity in the layer below the interface that is associated with the  $P_{i1P}$  reflection. If the velocities in this layer are too high then the theoretical traveltimes become too fast. On the other hand, if the velocities are too low then the velocity contrast across the interface becomes too small and there is little energy in the  $P_{i1P}$  reflection. For example, a model with a uniform velocity of  $6.2 \text{ km s}^{-1}$  in this layer produced almost no energy in the  $P_{i1P}$  reflection in the theoretical record sections for shots 3 and 4. For this reason, and to keep the traveltime data acceptably well fitted, the velocities in this layer vary laterally from lower values in the north to higher values in the south. A velocity of  $6.5 \text{ km s}^{-1}$  for this layer in the south produces acceptably high amplitudes for the  $P_{i1P}$  reflection in the theoretical record sections for shots 3 (Fig. 9) and 4.

### Step 3: lower crustal structure

In the third step of the modelling process, the interface depths associated with the intracrustal reflection  $P_{i2P}$  and the velocity in the lower crustal layer associated with the refraction  $P_{i2}$  were determined by inverting 34 traveltimes for the  $P_{i2P}$  phase and three traveltimes for the  $P_{i2}$  phase (Table 1). As the number of traveltime readings for these two phases is small, a 2-D starting model was used based on the 1-D modelling. The starting model had interface depths of 45 km below the surface in the south and 30 km below the surface in the north, with a smooth change between model km 130 and 230. It also had a velocity at the top of the lower crustal layer of  $6.7 \text{ km s}^{-1}$  in the south and  $6.5 \text{ km s}^{-1}$  in the north, with a smooth change between model km 90 and 270. As in the case of the top two layers, the velocities at the top and bottom of the layer were constrained to be updated by the same amount in each iteration of the inversion. Only two independent interface nodes, each with an *a priori* uncertainty of  $\pm 5$  km, and one independent velocity node, with an *a priori* uncertainty of  $\pm 0.3 \text{ km s}^{-1}$ , were utilized in the inversion (Tables 2 and 3).

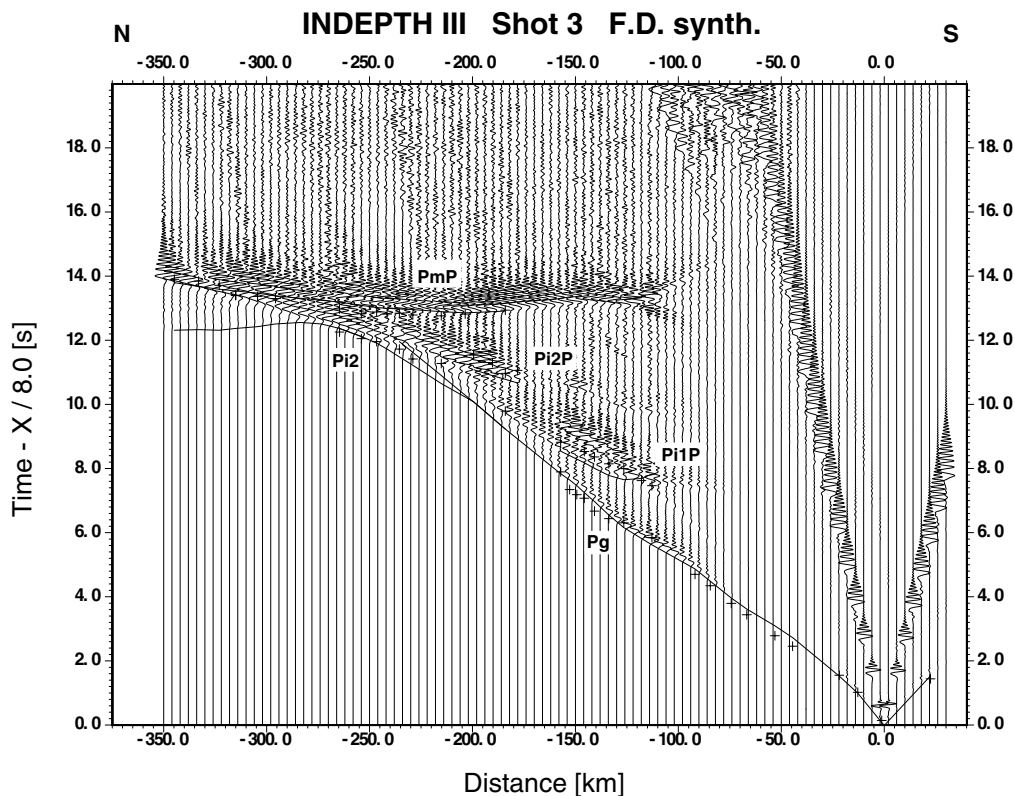


**Figure 9.** Synthetic seismogram section for shot 3 along the INDEPTH III profile. The record section reduced with a velocity of  $8 \text{ km s}^{-1}$  shows the vertical component of  $P$ -wave motion in which each trace is normalized individually. Continuous lines represent phases calculated from the model in Fig. 7, while crosses represent traveltimes from the observed data in Fig. 2. Key: see Fig. 2.

As the starting model was somewhat fast, the inversion increased the interface depths and decreased the velocities in the lower crustal layer. After five iterations both the interface depths and the velocity in the lower crustal layer had stopped changing and the average absolute traveltimes residual had decreased from 0.30 s in the starting model to 0.26 s. As would be expected from the very limited ray coverage through the lower crustal layer (Fig. 8c), only the two interface nodes are relatively well resolved (Table 2). The interface depths in the final model are 1.3 km greater than in the starting model in the south, and 1.1 km greater in the north. Although the velocity contrast between the middle and lower crustal layers is only  $0.1\text{--}0.5 \text{ km s}^{-1}$ , the amplitudes of the  $Pi2P$  reflection in the theoretical record section for shot 3 (Fig. 9) are acceptably high at distances similar to those where the phase is observed (Fig. 2).

#### Step 4: Moho structure

In the final step, 56 traveltimes readings (Table 1) for the reflected phase,  $PmP$ , were inverted to derive the crust–mantle boundary (Moho) structure. The 2-D starting model consisted of a horizontal interface at an average depth of about 65 km below the surface, and four independent interface nodes, each with an *a priori* uncertainty of  $\pm 5$  km (Tables 2 and 3). After six iterations the average absolute traveltimes residual had reduced from 0.29 s in the starting model to 0.27 s, and the outer two better resolved interface nodes had ceased to change. Thus the inversion was stopped at this point, with Moho depths of 66–67 km below the surface in the south and 64–65 km

below the surface in the north. The inversion also yielded a small change in Moho depths of 2–3 km, 25–50 km north of the surface trace of the Banggong–Nujiang suture.

The velocity in the lower crust immediately above the Moho is  $7.2\text{--}7.3 \text{ km s}^{-1}$  and the velocity contrast at the Moho is around  $0.7\text{--}0.8 \text{ km s}^{-1}$ . As noted above, the  $PmP$  phase has apparent velocities greater than  $7.0 \text{ km s}^{-1}$  at large offsets, and thus the values of  $7.2\text{--}7.3 \text{ km s}^{-1}$  shown in the model (Fig. 7) are compatible with this observation.

## DISCUSSION AND CONCLUSIONS

The crustal thickness beneath the INDEPTH III profile is  $65 \pm 5$  km with an indication of a shallowing of the Moho to the north by 2–3 km, 25–50 km north of the surface trace of the Banggong–Nujiang suture (BNS). The average crustal  $P$ -wave velocity varies from about  $6.3 \text{ km s}^{-1}$  in the south to around  $6.2 \text{ km s}^{-1}$  in the north, in contrast to a global average of  $6.45 \pm 0.21 \text{ km s}^{-1}$  (Christensen & Mooney 1995). The crustal thickness value is in agreement with the value of 65 km that Rodgers & Schwartz (1998) derived for the Qiangtang terrane from regional waveform modelling, and that Zhao *et al.* (1996) and Owens & Zandt (1997) obtained for the Qiangtang terrane from the seismic station WND0 about 300 km east of the INDEPTH III profile. It is also close to the 70 km value that Sapin *et al.* (1985) derived from an E–W profile, located mainly to the east of the INDEPTH III profile, in the northern Lhasa terrane just south of the BNS, and that Rodgers & Schwartz (1997) obtained for paths mainly through the Lhasa terrane in southern Tibet. However, the INDEPTH III profile shows no

evidence of a step in the Moho across the BNS of the order of 20 km as postulated by Hirn *et al.* (1984a) from fan profiling with Moho reflection points about 100 km east of the INDEPTH III profile. Rather, the 2–3 km decrease in crustal thickness along the INDEPTH III profile, 25–50 km north of the surface trace of the BNS, is in agreement with the decrease of about 4 km found in the vicinity of the BNS about 500 km to the west (Kong *et al.* 1996).

With respect to the average crustal *P*-wave velocity, Owens & Zandt (1997) obtained from the seismic station WNDO a value of 6.1 km s<sup>-1</sup>, which is somewhat lower than the values obtained from the INDEPTH III profile. The average crustal *P*-wave velocities obtained in this study are also higher than the values of 5.9–6.1 km s<sup>-1</sup> obtained from regional waveform modelling for paths mainly through the Lhasa terrane in southern Tibet (Rodgers & Schwartz 1997). However, they are in agreement with the values of 6.1–6.3 km s<sup>-1</sup> obtained for the Qiangtang terrane (Rodgers & Schwartz 1998). The two-way traveltime (TWT) to the Moho at model km 130 is about 21 s. At the same place, near-vertical incidence recordings were carried out within the framework of INDEPTH III (see above). From these recordings a stacked section has been produced which shows, at about 22 s TWT, a significant drop-off in reflectivity which, in conjunction with the wide-angle data presented here, is interpreted to represent the reflection Moho (Zhao *et al.* 1999).

The INDEPTH III profile shows evidence for a 20–35 km thick lower crustal layer with high velocities ranging from 6.5 to 6.6 km s<sup>-1</sup> at the top to 7.2–7.3 km s<sup>-1</sup> at the base. The E–W profile mentioned above (Sapin *et al.* 1985) shows a lower crustal layer almost 40 km thick with a velocity of 6.5 km s<sup>-1</sup> underlain by a crust–mantle transition zone about 10 km thick. For the seismic station WNDO, Owens & Zandt (1997) show a basal crustal layer about 15 km thick with velocities ranging from 6.3 km s<sup>-1</sup> at the top to 7.4 km s<sup>-1</sup> at the base. Thus while actual velocity and thickness values vary, all three seismic soundings in the region do show evidence of a basal crustal layer with high *P*-wave velocity.

The high velocities of the lower crustal layer can be compared with those derived from lower crustal xenoliths collected by INDEPTH III field geologists in the Qiangtang terrane almost 100 km northeast of the north end of the INDEPTH III seismic profile. The comparison (Hacker *et al.* 2000) shows overlap between the two sets of velocities, although, at any given depth, the INDEPTH III seismic velocities shown here are roughly 0.2 km s<sup>-1</sup> faster than those derived from the xenoliths. The mineralogies of the xenoliths indicate that the lower crustal layer is at ambient temperatures of 800–1100 °C and is composed chiefly of anhydrous meta-sedimentary rocks, less mafic granulite, and rare amphibolite and clinopyroxenite. The small difference between the seismic velocities and the calculated xenolith velocities suggests that faster, more mafic or refractory rocks are present in the Qiangtang lower crust and have not been erupted as xenoliths.

Sapin *et al.* (1985) introduced a layer with low *P*-wave velocity between about 20 and 24 km depth along the E–W profile mentioned above, in order to explain some high-amplitude reflections at short distances. In interpreting data from the same profile, Zhi & Wu (1987) introduced a low-velocity zone for both *P* and *S* waves between about 10 and 20 km depth. Neither the Owens & Zandt (1997) model for the seismic station WNDO nor the INDEPTH III model presented here shows

a crustal *P*-wave low-velocity zone. In view of the evidence for a mid-crustal low-velocity zone also for *P* waves from the INDEPTH II experiments within the Yadong–Gulu rift to the southeast of the INDEPTH III survey (Brown *et al.* 1996; Makovsky *et al.* 1996; Alsdorf *et al.* 1998b; Makovsky & Klemperer 1999), a model including a mid-crustal low-velocity layer has been tested on the INDEPTH III data. The results show that a model with a 10 km thick low-velocity zone with a velocity reduction of 0.1 km s<sup>-1</sup> with respect to the background velocity will also adequately fit the traveltime and amplitude data. However, it is necessary to reduce some interface depths by around 1 km to achieve this fit.

Owens & Zandt (1997) used an upper crustal velocity of 6.3 km s<sup>-1</sup> to model the data from the seismic station WNDO. This is considerably higher than the velocities in the model presented here (Fig. 7), and the upper crustal velocity of Owens & Zandt (1997) does not fit the INDEPTH III data. Although the seismic data from station WNDO have not been remodelled in the present study, it seems probable that use of a smaller upper crustal velocity would result in a thicker high-velocity lower crustal layer, as shown in the INDEPTH III model (Fig. 7), being required to fit the data.

Whereas the velocities of 5.9–6.2 km s<sup>-1</sup> for the upper crust beneath most of the INDEPTH III profile (Fig. 7) are within one standard deviation for average crust at 10 km depth worldwide (Christensen & Mooney 1995), the values of 5.6–5.7 km s<sup>-1</sup> in the vicinity of the BNS between model km 170 and 270 are anomalously low. A search of a data bank containing velocity measurements for 416 rocks of many different types (Stadtlander *et al.* 1999 and references therein) reveals that, amongst other rock types, serpentinite and spilite have such low velocities at 10–15 km depth. It is an attractive hypothesis to think that the low observed seismic velocities in the vicinity of the BNS could be explained as being due to a body of serpentinite and/or spilite. Alternatively, the rocks could be of the same composition as those to the north or south, and the anomalously low velocities could be due to the presence of more fluid-filled cracks in the vicinity of the BNS. A further possibility is that the low velocities represent a buried Mesozoic or Palaeozoic sedimentary basin.

The results presented here from the INDEPTH III wide-angle seismic experiment have been combined with other seismic results to construct a cross-section of Moho depths across Tibet (Fig. 10). This cross-section shows that crustal thickness tends to decrease from south to north, with values of 70–80 km south of the middle of the Lhasa terrane, 60–70 km in the northern part of the Lhasa terrane and the Qiangtang terrane, and less than 60 km in the Qaidam basin. This trace of the Moho is emphasized by the shaded band in the cross-section (Fig. 10). The bulk of the observations are incompatible with the large offsets in the Moho proposed by Hirn *et al.* (1984a). There is also considerable discrepancy as to the crustal thickness beneath the Songpan–Ganz terrane, with values ranging from 55 km (Herquel *et al.* 1995; Owens & Zandt 1997) to about 70 km (Lu & Wang 1990; Zhao *et al.* 1996). As the average topography of the plateau is essentially flat south of the Qaidam basin (Jin *et al.* 1994), and as the plateau is more or less in isostatic equilibrium (Molnar 1988; Jin *et al.* 1994), the northward decrease in crustal thickness implies that the average crustal density and/or the upper mantle density decreases northwards until the Qaidam basin is reached. A northward decrease in mantle density could support the hypothesis that the mantle

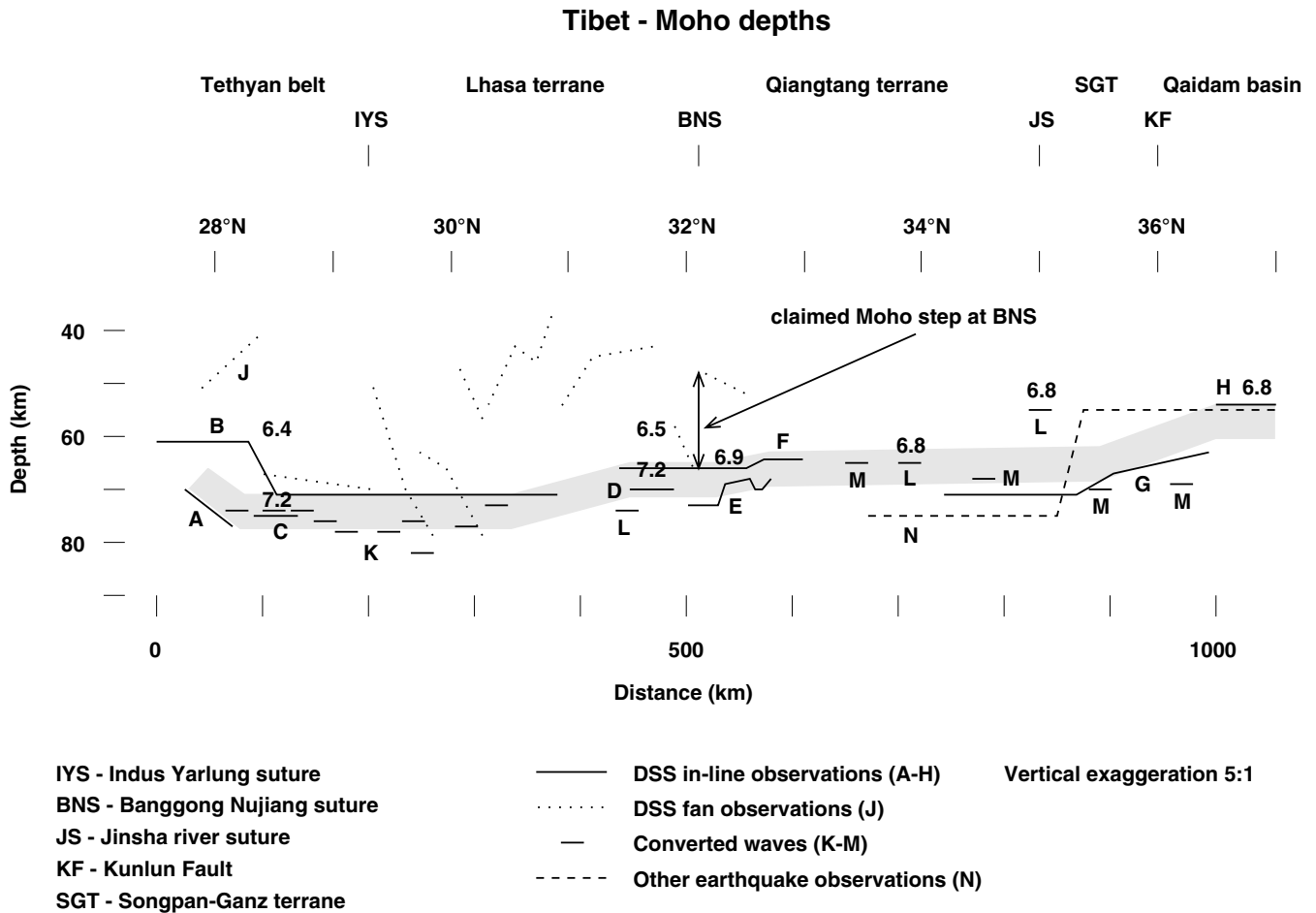


**Figure 10.** Cross-section showing Moho depths (below surface) across Tibet. This cross-section shows that crustal thickness tends to decrease from south to north as emphasized by the shaded band. Data, with letters following the references keyed to the measurements shown in the figure, are from Hirn *et al.* (1984a), J; Hirn *et al.* (1984b), C; Sapin *et al.* (1985), D; Yin *et al.* (1990), B; Lu & Wang (1990), G; Zhao *et al.* (1993), A; Gao *et al.* (1995), H; Herquel *et al.* (1995), N; Kong *et al.* (1996), E; Zhao *et al.* (1996), M; Kind *et al.* (1996), K; Yuan *et al.* (1997), K; Owens & Zandt (1997), L; and this study, F.

under northern Tibet south of the Qaidam basin is hotter than that under southern Tibet (Ni & Barazangi 1983; Molnar 1988). This is in turn consistent with the observations of a strongly attenuated high-frequency  $S_n$  phase (Ni & Barazangi 1983; McNamara *et al.* 1995) and strongly developed shear wave anisotropy (McNamara *et al.* 1994; Huang *et al.* 2000) under roughly the same portion of northern Tibet.

#### ACKNOWLEDGMENTS

For financial support during the project we thank the Ministry of Land and Resources of China, the National Natural Science Foundation of China, the US National Science Foundation (Grant Nos NSF-EAR-CD-9614616, NSF-EAR-CD-9614245, NSF-EAR-CD-9614853 and NSF-EAR-CD-9614890), the Deutsche Forschungsgemeinschaft, and the GeoForschungs-Zentrum Potsdam (GFZ). We are also very grateful to the personnel of the 5th Geophysical Exploration company of the Ministry of Land and Resources for their logistic support, and for drilling and executing the shots of the controlled-source survey. All field assistants are also thanked, as are the INDEPTH field geologists L. Ratschbacher and B. Hacker. The instruments were provided by IRIS-PASSCAL and the

GFZ Potsdam geophysical instrument pool. The traveltime and amplitude modelling was performed on the Hewlett-Packard parallel computers of the central computing facility of the GFZ Potsdam.

#### REFERENCES

- Allègre, C.J. *et al.*, 1984. Structure and evolution of the Himalaya-Tibet orogenic belt, *Nature*, **307**, 17–22.
- Alsdorf, D., Makovsky, Y., Zhao, W., Brown, L.D., Nelson, K.D., Klemperer, S., Hauck, M., Ross, A., Cogan, M., Clark, M., Che, J. & Kuo, J., 1998a. INDEPTH (International Deep Profiling of Tibet and the Himalaya) multichannel seismic reflection data: Description and availability, *J. geophys. Res.*, **103**, 26 993–26 999.
- Alsdorf, D., Brown, L., Nelson, K.D., Makovsky, Y., Klemperer, S. & Zhao, W., 1998b. Crustal deformation of the Lhasa terrane, Tibet plateau from Project INDEPTH deep seismic reflection profiles, *Tectonics*, **17**, 501–519.
- Brown, L.D., Zhao, W., Nelson, K.D., Hauck, M., Alsdorf, D., Ross, A., Cogan, M., Clark, M., Liu, X. & Che, J., 1996. Bright spots, structure, and magmatism in southern Tibet from INDEPTH seismic reflection profiling, *Science*, **274**, 1688–1690.
- Červený, V., Molotov, I.A. & Pšenčík, I., 1977. *Ray Method in Seismology*, University of Karlova, Prague.

- Christensen, N.I. & Mooney, W.D., 1995. Seismic velocity structure and composition of the continental crust: a global view, *J. geophys. Res.*, **100**, 9761–9788.
- Dewey, J.F., Shackleton, R.M., Chang, C. & Sun, Y., 1988. The tectonic evolution of the Tibetan plateau, *Phil. Trans. R. Soc. Lond., A*, **327**, 379–413.
- Fuchs, K. & Müller, G., 1971. Computation of synthetic seismograms with the reflectivity method and comparison with observations, *Geophys. J. R. astr. Soc.*, **23**, 417–433.
- Gao, R., Cheng, X.-Z. & Ding, Q., 1995. Preliminary geodynamic model of Golmud-Ejin Qi geoscience transect, *Acta Geophys. Sinica*, **38**, 3–14.
- Girardeau, J., Marcoux, J., Allègre, C.J., Bassoulet, J.P., Youking, T., Xuchang, X., Yougong, Z. & Xibin, W., 1984. Tectonic environment and geodynamic significance of the Neo-Cimmerian Donqiao ophiolite, Bangong-Nujiang suture zone, Tibet, *Nature*, **307**, 27–31.
- Hacker, B.R., Gnos, E., Ratschbacher, L., Grove, M., McWilliams, M., Sobolev, S.V., Jiang, W. & Wu, Z., 2000. Hot and dry deep crustal xenoliths from Tibet, *Science*, **287**, 2463–2466.
- Herquel, G., Wittlinger, G. & Guilbert, J., 1995. Anisotropy and crustal thickness of Northern-Tibet. New constraints for tectonic modelling, *Geophys. Res. Lett.*, **22**, 1925–1928.
- Hirn, A., Necessian, A., Sapin, M., Jobert, G., Xin, X.Z., Yuan, G.E., Jing, W.X., Yuan, L.D. & Wen, T.J., 1984a. Lhasa block and bordering sutures—a continuation of a 500-km Moho traverse through Tibet, *Nature*, **307**, 25–27.
- Hirn, A., Lepine, J.-C., Jobert, G., Sapin, M., Wittlinger, G., Xin, X.Z., Yuan, G.E., Jing, W.X., Wen, T.J., Bai, X.S., Pandey, M.R. & Tater, J.M., 1984b. Crustal structure and variability of the Himalayan border of Tibet, *Nature*, **307**, 23–25.
- Huang, W.-C., Ni, J.F., Tilmann, F., Nelson, D., Guo, J., Zhao, W., Mechie, J., Kind, R., Saul, J., Rapine, R. & Hearn, T.M., 2000. Seismic polarization anisotropy beneath the central Tibetan Plateau, *J. geophys. Res.*, **105**, 27 979–27 989.
- Jin, Y., McNutt, M.K. & Zhu, Y., 1994. Evidence from gravity and topography data for folding of Tibet, *Nature*, **371**, 669–674.
- Kelly, K.R., Ward, R.W., Treitel, S. & Alford, R.M., 1976. Synthetic seismograms: a finite difference approach, *Geophysics*, **41**, 2–27.
- Kidd, W.S.F., Pan, Y., Chang, C., Coward, M.P., Dewey, J.F., Gansser, A., Molnar, P., Shackleton, R.M. & Sun, Y., 1988. Geological mapping of the 1985 Chinese-British Tibetan (Xizang-Qinghai) plateau geotraverse route, *Phil. Trans. R. Soc. Lond., A*, **327**, 287–305.
- Kind, R., Ni, J., Zhao, W., Wu, J., Yuan, X., Zhao, L., Sandvol, E., Reese, C., Nabelek, J. & Hearn, T., 1996. Mid-crustal low velocity zone beneath the southern Lhasa block: Results from the INDEPTH-II earthquake recording program, *Science*, **274**, 1692–1694.
- Kong, X., Wang, Q. & Xiong, S., 1996. Comprehensive geophysics and lithospheric structure in the western Xizang (Tibet) Plateau, *Sci. China (Ser. D)*, **39**, 348–358.
- Lu, D. & Wang, X., 1990. The crustal structure and deep internal processes in the Tuotuohe-Golmud area of the north Qinghai-Xizang plateau, *Bull. Chinese Acad. geol. Sci.*, **21**, 227–237.
- Lutter, W.J. & Nowack, R.L., 1990. Inversion for crustal structure using reflections from the PASSCAL Ouachita experiment, *J. geophys. Res.*, **95**, 4633–4646.
- Lutter, W.J., Nowack, R.L. & Braille, L.W., 1990. Seismic imaging of upper crustal structure using travel times from the PASSCAL Ouachita experiment, *J. geophys. Res.*, **95**, 4621–4631.
- McNamara, D.E., Owens, T.J., Silver, P.G. & Wu, F.T., 1994. Shear wave anisotropy beneath the Tibetan Plateau, *J. geophys. Res.*, **99**, 13 655–13 665.
- McNamara, D.E., Owens, T.J. & Walter, W.R., 1995. Observations of regional phase propagation across the Tibetan Plateau, *J. geophys. Res.*, **100**, 22 215–22 229.
- Makovsky, Y. & Klemperer, S.L., 1999. Measuring the seismic properties of Tibetan bright spots: Evidence for free aqueous fluids in the Tibetan middle crust, *J. geophys. Res.*, **104**, 10 795–10 825.
- Makovsky, Y., Klemperer, S.L., Ratschbacher, L., Brown, L.D., Li, M., Zhao, W. & Meng, F., 1996. INDEPTH wide-angle reflection observation of P-wave-to-S-wave conversion from crustal bright spots in Tibet, *Science*, **274**, 1690–1691.
- Molnar, P., 1988. A review of geophysical constraints on the deep structure of the Tibetan Plateau, the Himalaya and the Karakorum, and their tectonic implications, *Phil. Trans. R. Soc. Lond., A*, **326**, 33–88.
- Murphy, M.A., Yin, A., Harrison, T.M., Dürr, S.B., Chen, Z., Ryerson, F.J., Kidd, W.S.F., Wang, X. & Zhou, X., 1997. Did the Indo-Asian collision alone create the Tibetan plateau?, *Geology*, **25**, 719–722.
- Ni, J. & Barazangi, M., 1983. High-frequency seismic wave propagation beneath the Indian Shield, Himalayan Arc, Tibetan Plateau and surrounding regions: high uppermost mantle velocities and efficient  $S_n$  propagation beneath Tibet, *Geophys. J. R. astr. Soc.*, **72**, 665–689.
- Owens, T.J. & Zandt, G., 1997. Implications of crustal property variations for models of Tibetan Plateau evolution, *Nature*, **387**, 37–43.
- Podvin, P. & Lecomte, I., 1991. Finite difference computation of traveltimes in very contrasted velocity models: a massively parallel approach and its associated tools, *Geophys. J. Int.*, **105**, 271–284.
- Reynolds, A.C., 1978. Boundary conditions for the numerical solution of wave propagation problems, *Geophysics*, **43**, 1099–1110.
- Rodgers, A.J. & Schwartz, S.Y., 1997. Low crustal velocities and mantle lithospheric variations in southern Tibet from regional Pnl waveforms, *Geophys. Res. Lett.*, **24**, 9–12.
- Rodgers, A.J. & Schwartz, S.Y., 1998. Lithospheric structure of the Qiangtang Terrane, northern Tibetan Plateau, from complete regional waveform modelling: Evidence for partial melt, *J. geophys. Res.*, **103**, 7137–7152.
- Sandmeier, K.-J., 1990. Untersuchung der Ausbreitungseigenschaften seismischer Wellen in geschichteten und streuenden Medien, *PhD thesis*, Karlsruhe University.
- Sapin, M., Wang, X.-J., Hirn, A. & Xu, Z.X., 1985. A seismic sounding in the crust of the Lhasa block, Tibet, *Ann. Geophys.*, **3**, 637–646.
- Schneider, W.A., Ranzinger, K.A., Balch, A.H. & Kruse, C., 1992. A dynamic programming approach to first arrival traveltime computation in media with arbitrarily distributed velocities, *Geophysics*, **57**, 39–50.
- Stadlander, R., Mechie, J. & Schulze, A., 1999. Deep structure of the southern Ural mountains as derived from wide-angle seismic data, *Geophys. J. Int.*, **137**, 501–515.
- Vidale, J., 1988. Finite-difference calculation of travel times, *Bull. seism. Soc. Am.*, **78**, 2062–2076.
- Xia, D., Zhang, P., Xu, G., Zhen, A. & Xie, Y., 1993. *Regional Geology of Xizang (Tibet) Autonomous Region*, Geological Publishing House, Beijing.
- Yin, Z., Teng, J. & Liu, H., 1990. The 2-D crustal structure study in the Yadong-Damxung region of the Xizang plateau, *Bull. Chinese Acad. geol. Sci.*, **21**, 239–245.
- Yuan, X., Ni, J., Kind, R., Mechie, J. & Sandvol, E., 1997. Lithospheric and upper mantle structure of southern Tibet from a seismological passive source experiment, *J. geophys. Res.*, **102**, 27 491–27 500.
- Zelt, C.A. & Smith, R.B., 1992. Seismic traveltime inversion for 2-D crustal velocity structure, *Geophys. J. Int.*, **108**, 16–34.
- Zhao, L.-S., Sen, M.K., Stoffa, P. & Frohlich, C., 1996. Application of very fast simulated annealing to the determination of the crustal structure beneath Tibet, *Geophys. J. Int.*, **125**, 355–370.
- Zhao, W., Nelson, K.D. & Project INDEPTH Team, 1993. Deep seismic reflection evidence for continental underthrusting beneath southern Tibet, *Nature*, **366**, 557–559.
- Zhao, W., Ross, A.R., Brown, L.D., Nelson, K.D., Klemperer, S., Haines, S., Mechie, J., Saul, J. & Guo, J., 1999. Seismic bright spots and partial melting under the Tibet Plateau, *EOS, Trans. Am. geophys. Un.*, **80**, F952.
- Zhi, M. & Wu, F.T., 1987. Nature of the upper crust beneath central Tibet, *Earth planet. Sci. Lett.*, **84**, 204–210.